

Water repellent Bi₂MoO₆ cotton fabric for implementing water-source purification

Jie Yue

Liaocheng University

Shaowang Tang

Liaocheng University

Bo Ge (✉ gebo11@163.com)

Liaocheng University <https://orcid.org/0000-0003-2504-7289>

Min Wang

Liaocheng University

Guina Ren

Yantai University

Xin Shao

Liaocheng University

Research Article

Keywords: Photocatalytic, Visible-light response, Superhydrophobic Bi₂MoO₆

Posted Date: March 26th, 2021

DOI: <https://doi.org/10.21203/rs.3.rs-331310/v1>

License:   This work is licensed under a Creative Commons Attribution 4.0 International License.

[Read Full License](#)

Abstract

As a low-budget, facile-availability and eco-friendly substrate material, cotton fabric after hydrophobic modification has been applied to sewage purification. While, a single superhydrophobic function is unable to decompose toxic water-soluble organic dye. In this paper, pathways are propounded for the simultaneous achievement of the removal of insoluble spilling oil and organic dye contaminants. Particularly, the hydrophobic ZnSnO_3 after stearic acid modification and Bi_2MoO_6 catalysts are introduced into the cotton fabric substrate through solution dip-coating. The durability of the prepared fabric suffers from the acid-base corrosion, thermal treatment and mechanical wear, meanwhile, it still exhibits remarkable water repellent ($\text{WCA} > 150^\circ$) property. Furthermore, the remarkable photocatalytic activity makes it possible for reusable degradation and the primary active species, namely the holes, to be verified by the radicals-capturing experiment.

Introduction

In terms of polarity difference, the major contaminant categories of aquatic ecosystems are generally classified into water-soluble and spilling oil (Ge et al. 2020; Yue et al. 2020; Ma et al. 2020; Yin et al. 2020). For the treatment of aquatic pollution, the ecosystem lacks adequate self-cleaning function. Therefore, adopting reasonable manual strategies to achieve oil-water separation from sewage is quite significant for implementing water purification (Zhou et al. 2013; Shang et al. 2020; Wang et al. 2019; Ge et al. 2020). Superhydrophobic function provides an opportunity for selective oil-water separation, which is beneficial to the whole water circulation system (Kang et al. 2014; Qin et al. 2019). The construction methods of superhydrophobic surface were generalized by the following types (Zhu et al. 2020; Boreyko et al. 2013; Han et al. 2018): the surface of superhydrophobic materials was accustomed to building rough construction via in situ modification sundry substrates, such as glass (Isakov et al. 2020; Long et al. 2017), copper wire mesh (Torresin et al. 2013; Li et al. 2020), magnesium alloy (Yin et al. 2020; Wu et al. 2017) and fabric (Sun et al. 2020; Yang et al. 2019), etc. Furthermore, through grafting superhydrophobic particles on rough substrates, a superhydrophobic surface could be obtained, which was easier to implement. Among various artificial hydrophobic substrates, water repellent fabric is regarded promising due to its low-budget and environmental non-toxicity (Fang et al. 2020; Bai et al. 2020; Xue et al. 2015). Therefore, synthesizing superhydrophobic fabric with the preeminent waterproof performance and durability is regarded as an effective strategy to achieve the selective removal oil spilling from the sewage.

While, water-soluble contaminants are unable to be treated by the single superhydrophobic function. How to realize the simultaneous removal of the water-soluble dye and insolubility oil spilling becomes a crucial strategy to mitigate the damage to ecological constellation. Zhu et al. (Zhu et al. 2020) prepared a superhydrophobic P25 nanoparticle and polydimethylsiloxane on alkaline-etched copper mesh (P25@PDMS@COM), achieving the combination of water-soluble contaminant degradation under ultraviolet irradiation and the removal of oil phase. While, the traditional titanium dioxide (P25) catalyst can only respond to ultraviolet light. To make the utmost of the visible light in solar energy, research on

appropriate photocatalysts possessing wide-range solar light response has raised widespread attention. Among the numerous semiconductor photocatalysts, bismuth molybdate (Bi_2MoO_6) has presented vast potential in multiple applications, relying on its features including controllable morphology, relatively narrow band-gap, eco-friendliness and remarkable thermal stability (Liu et al. 2020; Zhang et al. 2020; Kashfi-Sadabad et al. 2016). As a typical layered Aurivillius metal-oxide, it takes on sandwich structure and is mainly constructed by $(\text{MoO}_4)^{2-}$ perovskite slabs as well as $(\text{Bi}_2\text{O}_2)^{2+}$ slices (Salari et al. 2020; Mei et al. 2019; Wang et al. 2016). But the most regret is that the single photocatalytic function is unable to resolve the oil-phase pollution, achieving an incorporation function of water repellent and the photocatalytic function ought to be a feasible strategy.

Herein, superhydrophobic SA- ZnSnO_3 is prepared via stearic acid (SA) modified on the surface of zinc stannate (ZnSnO_3) particles, reducing the damage of traditional superhydrophobic solutions (mercaptan (Gao et al. 2020) and fluorine-containing (Ruan et al. 2014), etc) to the ecological environment. Then, the superhydrophobic SA- ZnSnO_3 and Bi_2MoO_6 loaded fabric (denoted as SH BM fabric) are fabricated via physical dip-coating, achieving the removal of the insoluble spilling oil and organic dye contaminants, meanwhile resolving the recovery troubles of the catalysts. The remarkable properties of oil-water separation and decomposing organic substances are simultaneously applied into practical, indicating that SH BM fabric has a vast development prospect. The prepared product has fierce response for the visible-light, and the degradation efficiency remains at 94 % after being used repetitively. The relevant energy band configuration of Bi_2MoO_6 catalysts is herein investigated in detail, and the holes serve as the main active species via the trapping experiment.

Experimental

Materials and chemicals

Bismuth nitrate pentahydrate [$\text{Bi}(\text{NO}_3)_3 \cdot 5\text{H}_2\text{O}$], 2-methylimidazole and $\text{Na}_2\text{SnO}_3 \cdot 3\text{H}_2\text{O}$, stearic acid were purchased from Aladdin Biochemical Technology Co., Ltd. Sodium molybdate dihydrate ($\text{Na}_2\text{MoO}_4 \cdot 2\text{H}_2\text{O}$) was obtained from Sinopharm Chemical Reagent Co., Ltd. $\text{Zn}(\text{NO}_3)_2 \cdot 6\text{H}_2\text{O}$ was supplied by Shanghai Titanchem Co., Ltd. The polydimethylsiloxane (PDMS) and curing agent were provided by Dow Corning Co., Ltd.

Fabrication of Bi_2MoO_6

1 mmol $\text{Bi}(\text{NO}_3)_3 \cdot 5\text{H}_2\text{O}$ was put in 15 mL ethylene glycol, after being mixed uniformly, 0.5 mmol $\text{Na}_2\text{MoO}_4 \cdot 2\text{H}_2\text{O}$ was continuously added in the above solution. About stirring for 20 min, it was transferred to a sealed reaction container at 160 °C for 12 h. The obtained precipitation was further purified and dried at 80 °C for 12 h.

Fabrication of ZnSnO_3

To synthesize the target product, the purpose of additive metal-organic framework ZIF-8 was utilized to provide Zn source. The detailed fabrication procedures were shown: firstly, 0.9 g $\text{Zn}(\text{NO}_3)_2 \cdot 6\text{H}_2\text{O}$ was dispersed into 30 mL methanol until transparent solution was formed (solution A). 1.6 g 2-methylimidazole was dissolved in 20 mL methanol (solution B), and was then gradually poured into the above solution A under stirring for 1 h. After aging for an overnight, the white precipitation was further purified, and dried at 80 °C for 12 h.

Subsequently, in order to obtain ZnSnO_3 particles, 0.6 mmol ZIF-8 was scattered into 5 mL ethanol driven by the ultrasound (the ultrasonic time was approximately 1 h). Besides, the $\text{Na}_2\text{SnO}_3 \cdot 3\text{H}_2\text{O}$ with an identical molar ratio was dissolved in 30 mL deionized water, and then ZIF-8 dispersion was added drop by drop. After reaction for 30 min, the oyster white solution was purified by deionized water and ethanol, after which it was dried completely in an oven. Subsequently, the $\text{ZnSn}(\text{OH})_6$ precursor was conducted at 250 °C for 4 h (the heating rate was about 1.5 °C/ min), aimed at dehydration.

Fabrication of SA- ZnSnO_3

0.2 g stearic acid was dissolved in 50 mL ethanol to form solution, and 80 mg ZnSnO_3 was further introduced into the above mixture accompanied with ultrasonic dispersion for 10 min. After being stirred for 24 h, the reaction substance was obtained after several times of centrifugal purification by ethanol and dried at 80°C for 6 h.

Fabrication of superhydrophobic Bi_2MoO_6 fabric

100 mg PDMS, 0.04 g curing agent, and 20 mL ethyl acetate were agitated to form a homogeneous solution. 60 mg Bi_2MoO_6 catalyst and 60 mg SA- ZnSnO_3 were dispersed into the above solution completely, and then, the pristine fabric (the size was about 4 cm × 4 cm) was immersed in the mixed solution to perform a physical sedimentation, after which it was dried at 120 °C for 1 h. The repeated sedimentation process was conducted for 5 times, aiming to aggrandize the load content of Bi_2MoO_6 catalyst. To achieve an absolutely cure, the final fabric was dried at 120 °C for 2 h.

Characterization

The qualitative and quantitative analysis of the crystal phase are researched by Bruker D8w X-ray diffractometer. The surface micro-morphology and phase component structure are analyzed by scanning electron microscope (Zeiss Company, FESEM) and transmission electron microscope (FEI Tecnai F30, TEM). The Fourier infrared spectrum analysis (Nicolet iS50, FTIR) is utilized to investigate molecular structure and chemical bonds. The thermogravimetric curves of ZnSnO_3 and SA- ZnSnO_3 are analyzed by the thermogravimetric analyzer (STA 449C, TG). The X-ray photoelectron spectroscopy (ESC PHI500, XPS) is adopted to research the valence state discrimination of relevant chemical elements. The energy dispersive spectrum analysis (EDS) is used to characterize the distribution and the content of surface elements. The photocatalytic activity of degrading contaminants is evaluated via UV-visible

spectrophotometer (752B). The photocurrent test, Mott-Schottky (MS) and Nyquist impedance spectrum (EIS) of Bi_2MoO_6 catalyst are detected by a three-electrode electrochemical workstation. The separation and recombination situation of photo-induced carrier is measured by the photoluminescence spectroscopy (FLS 920, PL). The optical property of as-synthesized Bi_2MoO_6 is determined on diffuse reflectance spectrum (UV-3600 spectrophotometer, DRS). Brunauer-Emmett-Teller surface analysis (Belsorp-max, BET) of Bi_2MoO_6 are utilized to study specific surface and porosity. The superhydrophobic property of SH BM fabric is measured by contact angle meter (KrüssDSA100).

Results And Discussion

The crystallographic structure of as-synthesized products is represented by XRD. Fig. 1a shows the XRD patterns of orthorhombic Bi_2MoO_6 , the 2θ value of apparent characteristic diffraction peaks at 28.25° , 32.61° , 47.15° and 55.56° , which are indexed to crystal planes of (131), (200), (260) and (331) (JCPDS card No.71-2086). The XRD diffraction pattern of $\text{ZnSn}(\text{OH})_6$ precursor, ZnSnO_3 and SA- ZnSnO_3 are shown in Fig. 1b. It can be observed that the crystalline structure of $\text{ZnSn}(\text{OH})_6$ precursor is excellent and the position of its characteristic peaks at 22.78° , 32.44° and 52.42° are corresponded with (200), (220) and (420) planes and well matched with the cubic phase of $\text{ZnSn}(\text{OH})_6$ (JCPDS card No.73-2384). There's no redundant impurity peak, and the result demonstrates that the purity of the synthesized $\text{ZnSn}(\text{OH})_6$ precursor is high. Observably, the XRD patterns of dehydration ZnSnO_3 take on no apparent intense peak because the structure of the ZnSnO_3 sample is amorphous. During the process of annealing treatment, dehydration of the $\text{ZnSn}(\text{OH})_6$ precursor occurs. The initial hydrogen-oxygen bonds (-H-O-) cause breakage, forming plentiful dangling bonds on the external surface and disturbing the inner lattice, and then the amorphous structure of ZnSnO_3 finally comes into being.

After superhydrophobic SA modification, the XRD results of SA- ZnSnO_3 indicate that an amorphous structure is retained. To investigate the situation of surface-grafted SA, the FTIR analysis of ZnSnO_3 and SA- ZnSnO_3 are performed in Fig. 1c. The FTIR characteristic absorption peak of SA- ZnSnO_3 appears approximately at $1340\text{-}1465\text{ cm}^{-1}$ and $2850\text{-}3000\text{ cm}^{-1}$, which respectively contributes to the bending and stretching vibration of -C-H- bonds. Besides, to further verify the successful graft of SA, the thermal treatment of nitrogen protected atmosphere at 800°C is conducted in Fig. 1d. There is an obvious thermal weight loss of about 8.6 % at 800°C , caused by the disappearance of SA. Therefore, combined with the above measurement analysis, the results show the successfully grafted SA on the surface of ZnSnO_3 products.

The SEM technique is utilized to reflect surface morphology of the as-prepared products. It can be seen from the low magnification image (Fig. 2a) that ZnSnO_3 shows uniform cubic morphology. Fig. 2b presents the high magnification morphological image of SA- ZnSnO_3 , which exhibits that plentiful irregular nanoparticles exist on the surface of cubes. Especially, each cube surface contains a porous structure, taking on the irregular hollow crystal-structure boxes. The elemental mapping image of SA-

ZnSnO₃ is carried out via an EDS analysis. As is presented in Fig. 2c, the element distribution of Zn, Sn and O are considerably uniform. Besides, the TEM analysis of SA-ZnSnO₃ is further investigated to determine its internal structure. In Fig. 2d, the dark border and whitish heartland is in stark contrast, whose conclusion precisely demonstrates that SA-ZnSnO₃ displays a hollow box structure. In order to analyze the electronic structure and chemical state of the SA-ZnSnO₃ nanoparticles, the relevant XPS analysis is employed. Fig. 2e displays the Sn 3d spectrum, the peak position occurs at 486.7 eV and 495.2 eV, which are assigned to the Sn 3d_{5/2} and 3d_{3/2}. The peak of binding energy of Sn 3d spinning orbits is consistent with the quintessential tetravalent Sn ionic (Sn⁴⁺) in ZnSnO₃.

The surface morphology of Bi₂MoO₆ photocatalyst is conducted by scanning electron microscope. Fig. 3a and b intuitively represent the low and high magnification morphological images, numerous smaller nanoparticles aggregate with each other to constitute the Bi₂MoO₆ particles. Fig. 3c depicts the XPS measurement of Bi 4f orbitals from the Bi₂MoO₆ products. The peaks sited at 158.9 eV and 164.2 eV in the Bi 4f spectrum are assigned to 4f_{7/2} and 4f_{5/2}. To dig deeper into the microstructure of the Bi₂MoO₆ catalyst, the TEM analysis is performed. Fig. 3d further verifies that the morphology of Bi₂MoO₆ is constructed by the accumulation of abundant smaller particles. Besides, the Fig. 3e shows the HRTEM image of Bi₂MoO₆ as well as the lattice fringes spacing of 3.16 nm and 2.74 nm, assigned to the crystal planes of (131) and (200). Selective electron diffraction analysis is used to calibrate the diffraction crystal planes of (131) and (200) in Fig. 3f. Besides, the diffraction ring spectrum indicates the polycrystalline structure of Bi₂MoO₆.

The surface micro-morphology of pristine fabric and superhydrophobic Bi₂MoO₆ fabric is investigated through FESEM. As displayed in Fig. 4a, the pristine fabric is constructed by the multitudinous transverse and longitudinal cross-linking of fibers. Noticeably, the high magnification SEM image of pristine fabric shows that the skeleton surface is fairly smooth. While, after loading the SA-ZnSnO₃ and Bi₂MoO₆ particles, rough nano-structures are formed on the fiber surface (Fig. 4b). Besides, the synergistic effect between the rough nano-structures on the fiber surface and superhydrophobic SA-ZnSnO₃ is contributed to the achievement of the superhydrophobic function. The EDS mapping is utilized to characterize the surface chemical compositions (Fig. 4c) and element distribution (Fig. 4d) of the superhydrophobic Bi₂MoO₆ fabric. The content of elements including C, O, Zn, Sn, Bi and Mo of SH BM fabric is 43.9 %, 45.9 %, 4.7 %, 4.8 %, 0.3 % and 0.4 %, respectively. It can be observed that the elements of zinc (Zn) and molybdenum (Mo) are uniformly distributed, and this phenomenon demonstrates that the internal skeleton of the fabric is covered by SA-ZnSnO₃ and Bi₂MoO₆ particles.

To investigate the photocatalytic activity, the photodegradation experiment of SH BM fabric (4 cm × 4 cm) is conducted under visible-light irradiation. Fig. 5a shows the recycle degradation RhB solution (50 mL, 10 mg/L) of SH BM fabric, and a remarkable degradation efficiency is still maintained after going through four cycles of degradation tests (the degradation efficiency is higher than 94 %). Subsequently, to research the degradation circumstance of the SH BM fabric under the natural sunlight, the identical scale

superhydrophobic fabric is utilized to carry on the outdoor sunlight photocatalytic tests (Fig. 5b). The preeminent catalytic property is contributed to the organic dye contaminants resolved into nontoxic single molecules. The relevant photocatalytic reaction mechanism is explored through the active species capture experiments of Bi_2MoO_6 powder (Fig. 5c). Edetate disodium (0.5 mmol/L, EDTA-2Na), isopropyl alcohol (1 mmol/L, IPA) and p-Benzoquinone (1 mmol/L, p-BQ) respectively serve as the quenchers of vacancy (h^+), hydroxyl free radical ($\cdot\text{OH}$) and superoxide anion ($\cdot\text{O}_2^-$) (Yue et al. 2021; Tang et al. 2020; Deng et al. 2020; Li et al. 2019). The RhB solution (50 mL, 10 mg/L) is regarded as the principal degradation target, and the above scavengers are appended in the reaction system to investigate the principles of photocatalytic response. Correspondingly, Fig. 5d is the column chart of degradation efficiency with various scavengers added in reaction system. Compared with non-scavengers (99.7 %), the degradation efficiency of the additive IPA (99.6 %) and p-BQ (93.1 %) has barely changed, while it significantly decreases after adding EDTA-2Na (19.9 %) into the mixed solution. This result intuitively reflects that h^+ is the major active species that plays a crucial character in the entire photocatalytic reaction process.

Fig. 6a represents the adsorption-desorption isotherms of Bi_2MoO_6 , and the typical IV-type curves present hysteresis loops at the medium relative pressures (P/P_0) area, demonstrating the existence of abundant mesopores in Bi_2MoO_6 . Characterized by the BET analysis, the specific surface area of Bi_2MoO_6 is $65.801 \text{ m}^2 \text{ g}^{-1}$. Fig. 6b shows that the primary pore size distributions of Bi_2MoO_6 is approximately at 13.7 nm, further verifying the structure of the mesopores materials. The sequence photographs of removal oil phase (methylbenzene, dyed by oil red) are displayed in Fig. 6c. As is presented in the diagram, a facile oil skimmer is fabricated and applied to selective oil-water separation, exhibiting the phenomenon that the oil floating on the water surface is entirely picked up by the oil skimmer. The behavior of water phase (dyed by RhB) on the SH BM fabric surface is researched in Fig. 6d. The spherical water is standing on the as-synthesized sample, and the static contact angle indicates that the superhydrophobic performance of the SH BM fabric is pretty remarkable, as is shown in the illustration. Subsequently, to research the resistance stability of the SH BM fabric to acid and alkali corrosion, the samples are soaked in solutions of diverse pH values, namely 3, 5, 7, 9, 11 and 13. As is depicted in Fig. 6e, the water contact angles (WCA) remain surpassing 150° , therefore, the hydrophobic stability of the SH BM fabric is advantageous in the rigorous atmosphere.

In order to evaluate the superhydrophobic stability of SH BM fabric, it has been subjected to various harsh treatments. During the treatment process at a temperature of 100°C , the fabric samples are taken out with an interval of about 30 min. After dried at 120°C for 2 h, the water contact angles are detected to characterize the infiltration degree. As is displayed in Fig. 7a, it can be discovered that the water contact angles of SH BM fabric remain larger than a baseline degree of 150° after undergoing a series of high-temperature treatments.

In addition, the mechanical stability is explored by frictional wear experiment (Fig. 7b). The type of friction pair is a $\varnothing 6$ bearing steel ball and the supplementary loading is 1 N, with 200, 300, 400, 500 and

600 friction cycles conducted. The images of water on the SH BM fabric appear spherical, hence the results obviously indicate that the sample is of a remarkably durable superhydrophobic stability. To investigate the relevant relation between the polarization signal excitation of electricity and potential, a series of electrochemical measurements are performed in the article. Fig. 7c shows the electrochemical impedance spectroscopy of Bi_2MoO_6 powder, in which Z' and Z'' represent real and imaginary component of impedance. The photoluminescence spectra is utilized to investigate the photocatalytic activity and separation efficiency of photogenic carriers. As is displayed in the illustration, under the excitation wavelength of 298 nm, the electrons among the Bi_2MoO_6 catalyst in the upper state fall back to the ground state, generating the maximum emission wavelength of 468 nm. Furthermore, the photocurrent response is utilized to research the recombination mechanism of relevant electron-hole pairs (Fig. 7d). It is worth noting that the photocurrent value of Bi_2MoO_6 raises to a stable region when the light source is opened instantly, attributing to cathodic photocurrent signals generated by photo-induced electron transitions. Besides, the photocurrent signals show a photo-dependent performance, whose concrete expression is annihilated accompanied with the light source shutoff.

To determine the mechanism of photocatalytic activity, the relevant electronic band-gap structure of Bi_2MoO_6 is investigated. As is shown in Fig. 8a, the positive slope of the Mott-Schottky curves demonstrates that Bi_2MoO_6 is a typical n-type semiconductor, and the intercept of the abscissa axis represents that the value of flat band potential is about -0.925 eV. Correspondingly, the flat band potential is estimated to be -0.68 eV (vs. NHE). In Fig. 8b, the XPS valance band spectra are utilized to obtain the valance band information. From the valance band diagram, it can be summarized that the distance between the valance band and the flat band potential is determined to be 1.76 eV, therefore, the position of valance band (VB) is calculated to be 1.08 eV. In addition, to research the light-absorption property and the bandgap energy of the Bi_2MoO_6 catalyst, the UV-Vis diffuse reflectance analysis is performed. As is shown in Fig. 8c, it is noteworthy that the visible-light absorption edge of Bi_2MoO_6 is approximately 540 nm. Besides, according to the illustration of the $(\alpha h\nu)^2$ versus $h\nu$, the band gap energy (E_g) is calculated to be about 2.72 eV. Therefore, combined with the above calculation, the position of the conduction band (CB) is evaluated to be -1.64 eV.

Based on the above calculation and the analysis of energy band structure, the rational photocatalytic enhanced mechanism diagram of Bi_2MoO_6 is given in Fig. 8d. In this paper, RhB solution is regarded as the primary degradation target contaminant, and the oxidation-reduction ability of Bi_2MoO_6 semiconductor catalyst is utilized to decompose into eco-friendly components (H_2O , CO_2 , etc). Driven by the irradiation of visible-light, the electrons (e^-) of VB acquire energy to struggle free of forbidden band barriers and finally form an equal number of holes. The numerous aggregation h^+ of VB can oxidize aromatic structure dyes, therefore, the existence of h^+ is extremely crucial in the entire RhB degradation process.

Conclusion

Herein, the stearic acid modified ZnSnO₃ superhydrophobic nanoparticles and Bi₂MoO₆ catalysts are deposited on the surface layer of the cotton fabric via a facile dip-coating solution. The as-prepared SH BM fabric exhibits a preeminent superhydrophobic and photodegradation performance, which are simultaneously utilized to selective oil-water separation and the degradation of organic contaminants from sewage. No matter in what a harsh environment (thermal, acid and alkali corrosion as well as mechanics abrasion), the SH BM fabric is always of an excellent water non-wetting behavior, and its durability makes the multiple reusability realized. Furthermore, the photocatalytic stability of SH BM fabric is quite remarkable, whose degradation efficiency is still approximately 94 % after suffering cyclic application.

Declarations

Acknowledgements

The authors acknowledge the Natural Science Foundation of Shandong Province (Grant No. ZR2019PB017).

References

- Bai WB, Lin HM, Chen KH, Xu J, Chen JP, Zhang XM, Zeng RP, Lin JH, Xu YL (2020) Eco-friendly stable cardanol-based benzoxazine modified superhydrophobic cotton fabrics for oil-water separation. *Sep Purif Technol* 253:117545. <https://doi.org/10.1016/j.seppur.2020.117545>
- Boreyko JB, Srijanto BR, Nguyen TD, Vega C, Fuentes-Cabrera M, Collier CP (2013) Dynamic defrosting on nanostructured superhydrophobic surfaces. *Langmuir* 29:9516-9524. <https://dx.doi.org/10.1021/la401282c>
- Deng YC, Liu J, Huang YB, Ma MM, Liu K, Dou XM, Wang ZJ, Qu SC, Wang ZG (2020) Engineering the photocatalytic behaviors of g/C₃N₄-based metal-free materials for degradation of a representative antibiotic. *Adv Funct Mater* 31:2002353. <https://doi.org/10.1002/adfm.202002353>
- Fang YF, Liu C, Li M, Miao XM, Pei YB, Yan Y, Xiao WJ, Wu LB (2020) Facile generation of durable superhydrophobic fabrics toward oil/water separation via thiol-ene click chemistry. *Ind Eng Chem Res* 59:6130-6140. <https://dx.doi.org/10.1021/acs.iecr.9b06761>
- Gao RX, Liu X, Zhang TC, Ouyang LK, Liang Y, Yuan SJ (2020) Superhydrophobic copper foam modified with n-dodecyl mercaptan-CeO₂ nanosheets for efficient oil/water separation and oil spill cleanup. *Ind Eng Chem Res* 59:21510-21521. <https://dx.doi.org/10.1021/acs.iecr.0c04515>
- Ge B, Ren GN, Yang H, Yang JJ, Pu XP, Li WZ, Jin CY, Zhang ZZ (2020) Fabrication of BiOBr-silicone aerogel photocatalyst in an aqueous system with degradation performance by sol-gel method. *Sci China Technol Sc* 63:859-865. <https://doi.org/10.1007/s11431-019-1499-x>

- Ge B, Zhang YL, Zhang TX, Ren GN, Li WZ, Zhao H (2020) Construction of superhydrophobic directly Z-scheme bismuth oxybromide/silver phosphate fabric surface with UV shielding and enhanced visible light absorption activity. *Sci China Technol Sc* 63. <https://doi.org/10.1007/s11431-020-1703-7>
- Han SW, Kim HJ, Woo TG, Jeong JH, Cha BJ, Kim YD (2018) Superhydrophobic fabric resistant to an aqueous surfactant solution as well as pure water for the selective removal of spill oil. *ACS Appl Mater Interfaces* 1:5158-5168. <https://dx.doi.org/10.1021/acsanm.8b01223>
- Isakov K, Kauppinen C, Franssila S, Lipsanen H (2020) Superhydrophobic antireflection coating on glass using grass-like alumina and fluoropolymer. *ACS Appl Mater Interfaces* 12:49957-49962. <https://dx.doi.org/10.1021/acсами.0c12465>
- Kang SM, Hwang S, Jin SH, Choi CH, Kim J, Park BJ, Lee D, Lee CS (2014) A rapid one-step fabrication of patternable superhydrophobic surfaces driven by marangoni instability. *Langmuir* 30:2828-2834. <https://dx.doi.org/10.1021/la500266f>
- Kashfi-Sadabad R, Yazdani S, Alemi A, Huan TD, Ramprasad R, Pettes MT (2016) Block copolymer-assisted solvothermal synthesis of hollow Bi_2MoO_6 spheres substituted with samarium. *Langmuir* 32:10967-10976. <https://doi.org/10.1021/acs.langmuir.6b02854>.
- Li LL, Yin XL, Sun YQ (2019) Facile synthesized low-cost MoS_2/CdS nanodots-on-nanorods heterostructures for highly efficient pollution degradation under visible light irradiation. *Sep Purif Technol* 212:135-141. <https://doi.org/10.1016/j.seppur.2018.11.032>
- Liu X, Huang WY, Zhou Q, Chen XR, Yang K, Li D, Dionysiou DD (2020) Ag-decorated 3D flower-like $\text{Bi}_2\text{MoO}_6/\text{rGO}$ with boosted photocatalytic performance for removal of organic pollutants. *Rare Met* <https://doi.org/10.1007/s12598-020-01574-3>
- Li ZK, He HQ, Liang Y, Ouyang LK, Zhang TC, Yuan SJ (2020) Photocatalytically driven self-cleaning and underwater superoleophobic copper mesh modified with hierarchical $\text{Bi}_2\text{WO}_6/\text{CuO}$ nanowires for oil/water separation. *Ind Eng Chem Res* 59:16450-16461. <https://dx.doi.org/10.1021/acsiacr.0c03101>
- Long MY, Peng S, Yang XJ, Deng WS, Wen N, Miao K, Chen GY, Miao XR, Deng WL (2017) One-step fabrication of non-fluorinated transparent super-repellent surfaces with tunable wettability functioning in both air and oil. *ACS Appl Mater Interfaces* 9:15857-15867. <https://dx.doi.org/10.1021/acсами.7b01926>
- Ma WJ, Ding YC, Zhang MJ, Gao ST, Li YS, Huang CB, Fu GD (2020) Nature-inspired chemistry toward hierarchical superhydrophobic, antibacterial and biocompatible nanofibrous membranes for effective UV-shielding, self-cleaning and oil-water separation. *J Hazard Mater* 384:121476. <https://doi.org/10.1016/j.jhazmat.2019.121476>
- Mei FF, Zhang JF, Dai K, Zhu GP, Liang CH (2019) A Z-scheme $\text{Bi}_2\text{MoO}_6/\text{CdSe}$ -diethylenetriamine heterojunction for enhancing photocatalytic hydrogen production activity under visible light. *Dalton Trans*

48:1067-1074. <https://doi.org/10.1039/c8dt04578j>

Qin LM, Chu Y, Zhou X, Pan QM (2019) Fast healable superhydrophobic material, *ACS Appl Mater Interfaces* 11:29388-29395. <https://dx.doi.org/10.1021/acsami.9b07563>

Ruan CP, Ai KL, Li XB, Lu LH (2014) A superhydrophobic sponge with excellent absorbency and flame retardancy. *Angew Chem Int Ed* 53:5556-5560. <https://dx.doi.org/10.1002/anie.201400775>

Salari H (2020) Facile synthesis of new Z-scheme $\text{Bi}_2\text{WO}_6/\text{Bi}_2\text{MoO}_6$ p-n junction photocatalysts with high photocatalytic activity: structure, kinetics and mechanism approach. *Mater Res Bull* 131:110979. <https://doi.org/10.1016/j.materresbull.2020.110979>

Shang QQ, Liu CG, Chen JQ, Yang XH, Hu Y, Hu LH, Zhou YH, Ren XL (2020) Sustainable and robust superhydrophobic cotton fabrics coated with castor oil-based nanocomposites for effective oil-water separation. *ACS Sustainable Chem Eng* 8:7423-7435. <https://dx.doi.org/10.1021/acssuschemeng.0c01469>

Sun YH, Huang JX, Guo ZG (2020) A CVD-assisted modification approach for preparing a dual superlyophobic fabric with in-air superhydrophobicity and underwater superoleophobicity. *Langmuir* 36:5802-5808. <https://dx.doi.org/10.1021/acs.langmuir.0c00504>

Tang YX, Zhang X, Ma YX, Wang XT, Su CH, Zhang DF, Pu XP, Geng YL (2020) One-dimensional core-shell $\text{Zn}_{0.1}\text{Cd}_{0.9}\text{S}/\text{SnIn}_4\text{S}_8$ heterojunction for enhanced visible light photocatalytic degradation. *Sep Purif Technol* 230:115856. <https://doi.org/10.1016/j.seppur.2019.115896>

Torresin D, Tiwari MK, Col DD, Poulikakos D (2013) Flow condensation on copper-based nanotextured superhydrophobic surfaces. *Langmuir* 29:840-848. <https://dx.doi.org/10.1021/la304389s>

Wang DJ, Shen HD, Guo L, Wang C, Fu F, Liang YC (2016) La and F co-doped Bi_2MoO_6 architectures with enhanced photocatalytic performance via synergistic effect. *RSC Adv* 6:71052-71060. <https://doi.org/10.1039/c6ra12898j>

Wang M, Peng M, Weng YX, Li YD, Zeng JB (2019) Toward durable and robust superhydrophobic cotton fabric through hydrothermal growth of ZnO for oil/water separation. *Cellulose* 26:8121-8133. <https://doi.org/10.1007/s10570-019-02635-2>

Wu CQ, Liu Q, Chen RR, Liu JY, Zhang HS, Li RM, Takahashi K, Liu PL, Wang J (2017) Fabrication of ZIF-8@ SiO_2 micro/nano hierarchical superhydrophobic surface on AZ31 magnesium alloy with impressive corrosion resistance and abrasion resistance. *ACS Appl Mater Interfaces* 9:11106-11115. <https://dx.doi.org/10.1021/acsami.6b16848>

Xue CH, Guo XJ, Ma JZ, Jia ST (2015) Fabrication of robust and antifouling superhydrophobic surfaces via surface-initiated atom transfer radical polymerization. *ACS Appl Mater Interfaces* 7:8251-8259.

<https://doi.org/10.1021/acsami.5b01426>

Yang YY, Huang W, Guo ZP, Zhang SY, Wu F, Huang JJ, Yang HJ, Zhou YS, Xu WL, Gu SJ (2019) Robust fluorine-free colorful superhydrophobic PDMS/NH₂MIL-125(Ti)@cotton fabrics for improved ultraviolet resistance and efficient oil-water separation. *Cellulose* 26:9335-9348. <https://doi.org/10.1007/s10570-019-02707-3>

Yin XX, Mu P, Wang QT, Li J (2020) Superhydrophobic ZIF-8-based dual-layer coating for enhanced corrosion protection of Mg alloy. *ACS Appl Mater Interfaces* 12:35453-35463. <https://dx.doi.org/10.1021/acsami.0c09497>

Yin YY, Zhu L, Chang X, Xue JW, Yu SF, Li XF, Xue QZ (2020) Bioinspired anti-oil-fouling hierarchical structured membranes decorated with urchin-like α -FeOOH particles for efficient oil/water mixture and crude oil-in-water emulsion separation. *ACS Appl Mater Interfaces* 12:50962-50970. <https://dx.doi.org/10.1021/acsami.0c11677>

Yue J, Wen GC, Ren GN, Tang SW, Ge B, Zhao LM, Shao X (2021) Superhydrophobic self-Supporting BiOBr aerogel for wastewater purification. *Langmuir* 37:406-416. <https://dx.doi.org/10.1021/acs.langmuir.0c03053>

Yue J, Yuan M, Zhang X, Wen GC, Ren GN, Ge B, Zhao LM, Shao X (2020) Fabrication of novel superhydrophobic ZIF-8 modified directly Z-scheme bismuth oxyiodide/cadmium sulfide melamine sponge for efficient oil/water separation and visible-light photodegradation. *Colloid Surface A* 601:124992. <https://doi.org/10.1016/j.colsurfa.2020.124992>

Zhang L, Shen QH, Yu LX, Huang FL, Zhang CT, Sheng JS, Zhang F, Cheng D, Yang H (2020) Fabrication of a high-adsorption N-TiO₂/Bi₂MoO₆ composite photocatalyst with a hierarchical heterostructure for boosted weak-visible-light photocatalytic degradation of tetracycline. *CrystEngComm* 22:5481-5490. <https://doi.org/10.1039/d0ce00761g>

Zhou XY, Zhang ZZ, Xu XH, Guo F, Zhu XT, Men XH, Ge B (2013) Robust and durable superhydrophobic cotton fabrics for oil/water separation. *ACS Appl Mater Interfaces* 5:7208-7214. <https://dx.doi.org/10.1021/am4015346>

Zhu H, Wu LZ, Meng X, Wang YQ, Huang Y, Xia F (2020) Anti-UV superhydrophobic material with photocatalysis, self-cleaning, self-healing and oil/water separation. *Nanoscale* 12:11455-11459. <https://doi.org/10.1039/D0NR01038C>

Zhu RF, Liu MM, Hou YY, Zhang LP, Li M, Wang D, Fu SH (2020) One-pot preparation of fluorine-free magnetic superhydrophobic particles for controllable liquid marbles and robust multifunctional coatings. *ACS Appl Mater Interfaces* 12:17004-17017. <https://dx.doi.org/10.1021/acsami.9b22268>

Figures

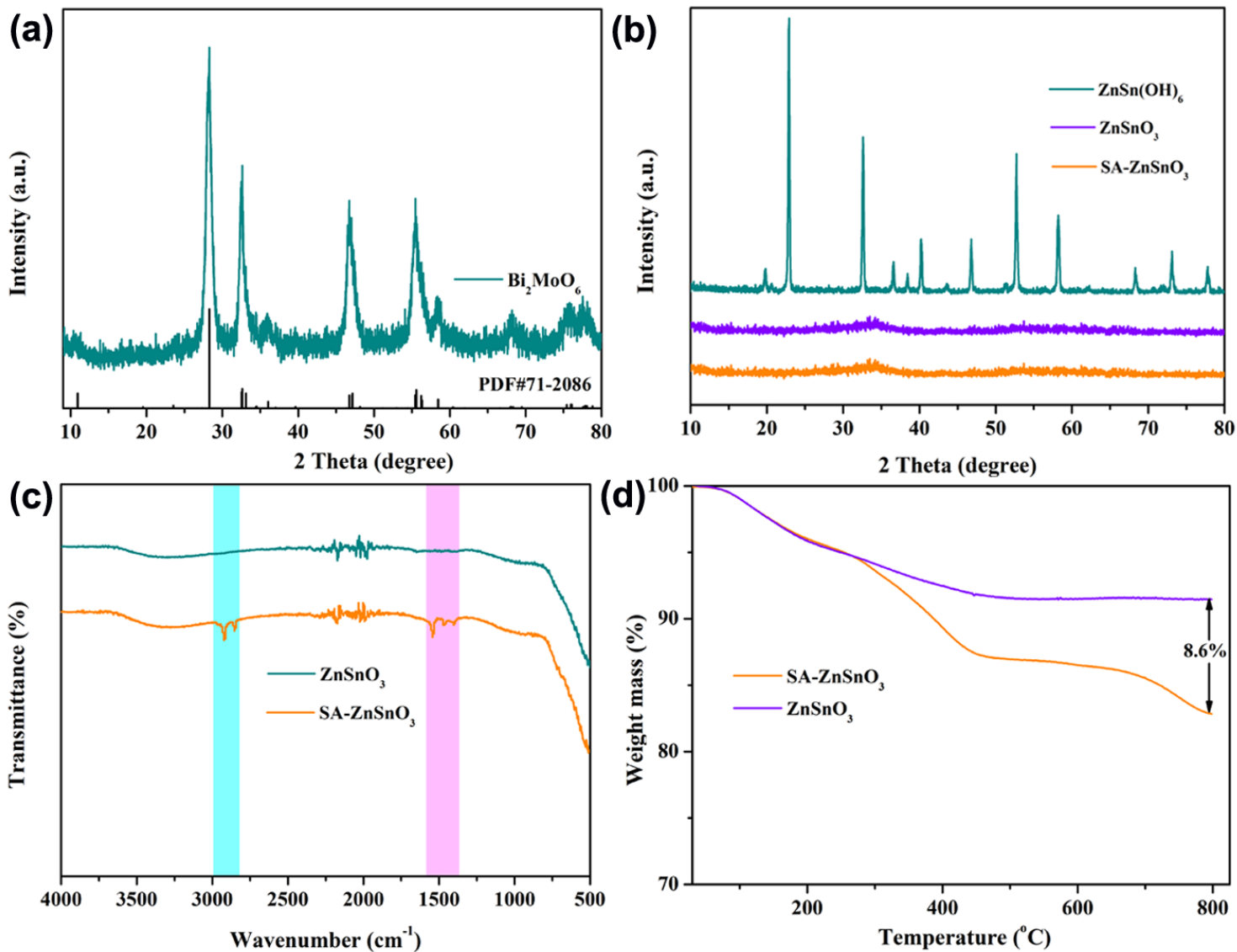


Figure 1

The XRD patterns: (a) Bi₂MoO₆, (b) ZnSn(OH)₆ precursor, ZnSnO₃ and SA-ZnSnO₃; (c) the FTIR spectrum analysis; (d) the TG curves of ZnSnO₃ and SA-ZnSnO₃ at the nitrogen protected atmosphere.

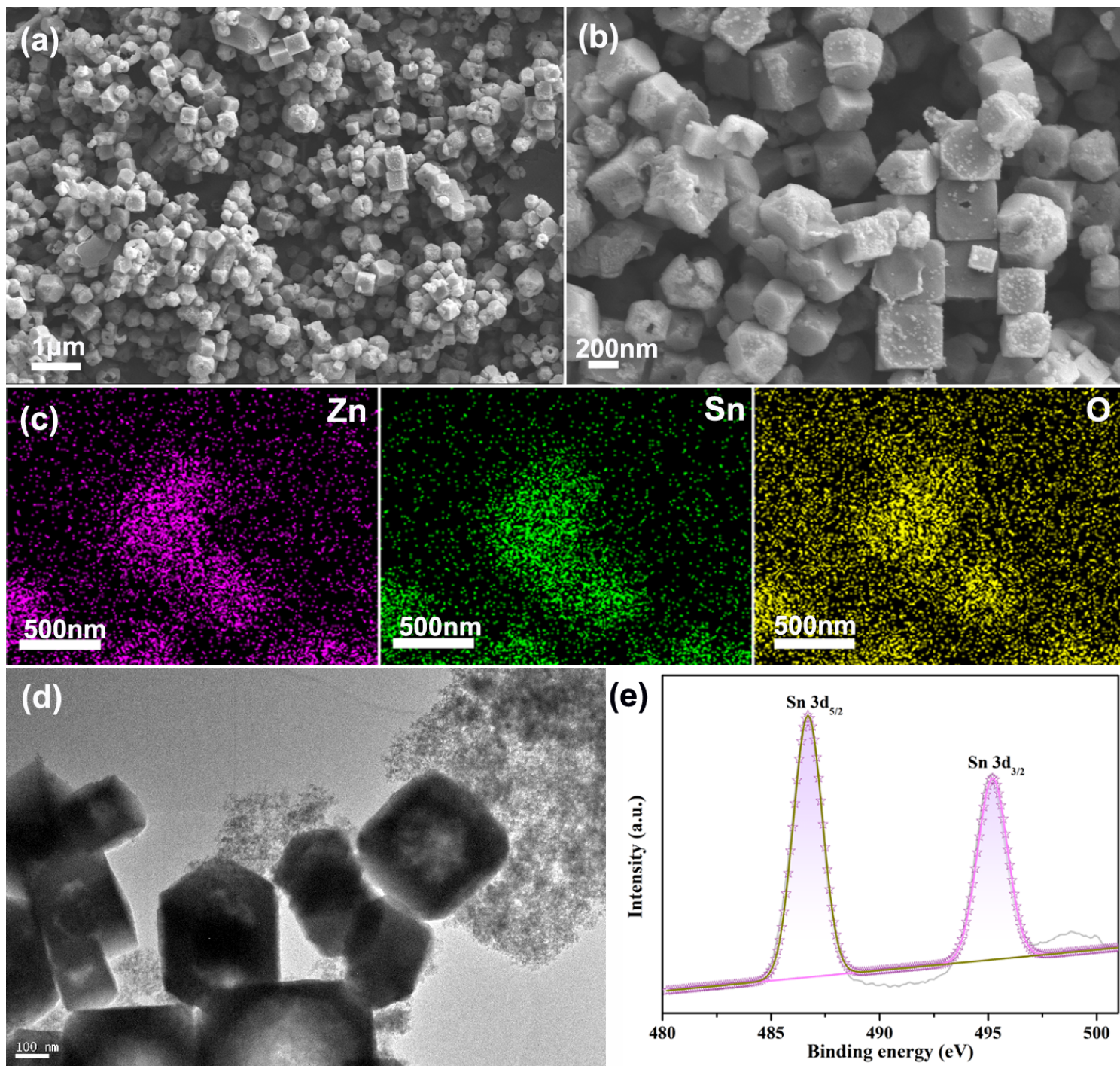


Figure 2

(a)-(b) various magnification morphological images of SA-ZnSnO₃; (c) the element distribution of Zn, Sn and O; (d) TEM characterization analysis of the SA-ZnSnO₃; (e) XPS spectrum of Sn 3d.

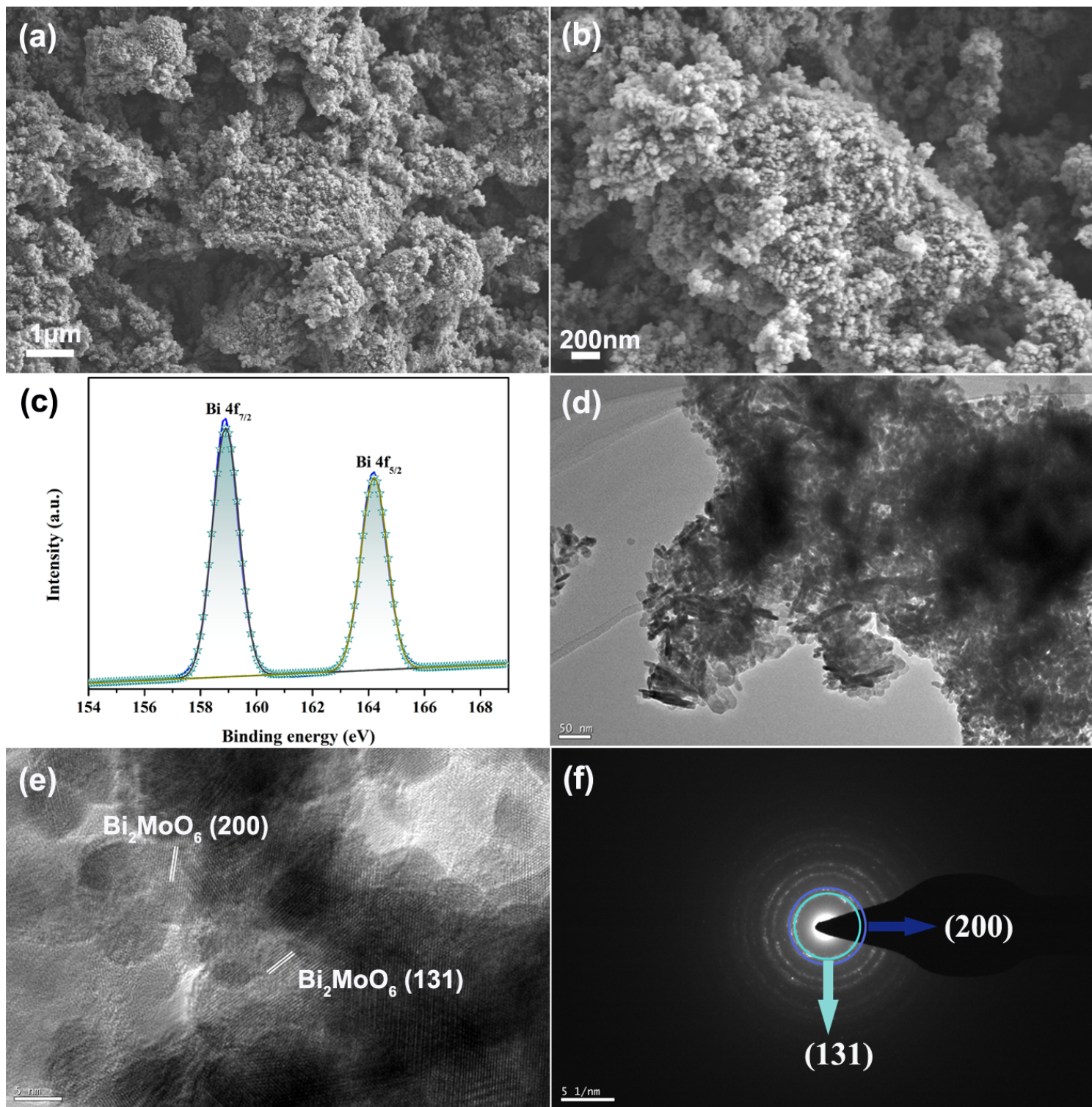


Figure 3

(a)-(b) The low and high magnification morphological images of Bi₂MoO₆ particles; (c) XPS spectrum of Bi 4f; (d)-(e) TEM and HRTEM analysis of Bi₂MoO₆; (f) the selective electron diffraction patterns of Bi₂MoO₆.

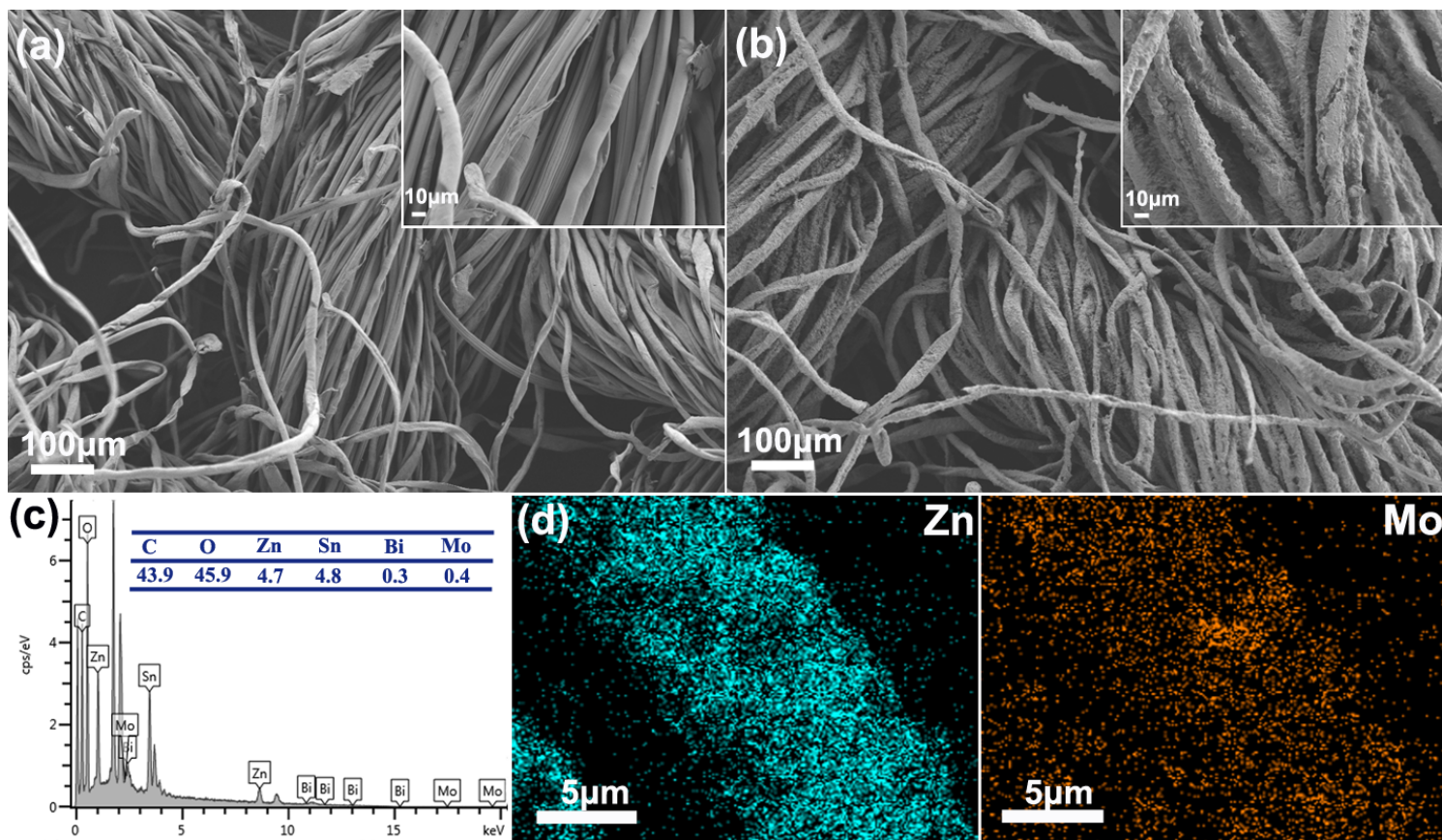


Figure 4

(a) FESEM images of the pristine fabric; (b) SH BM fabric; (c) the surface compositions of SH BM fabric; (d) the element mapping of Zn and Mo.

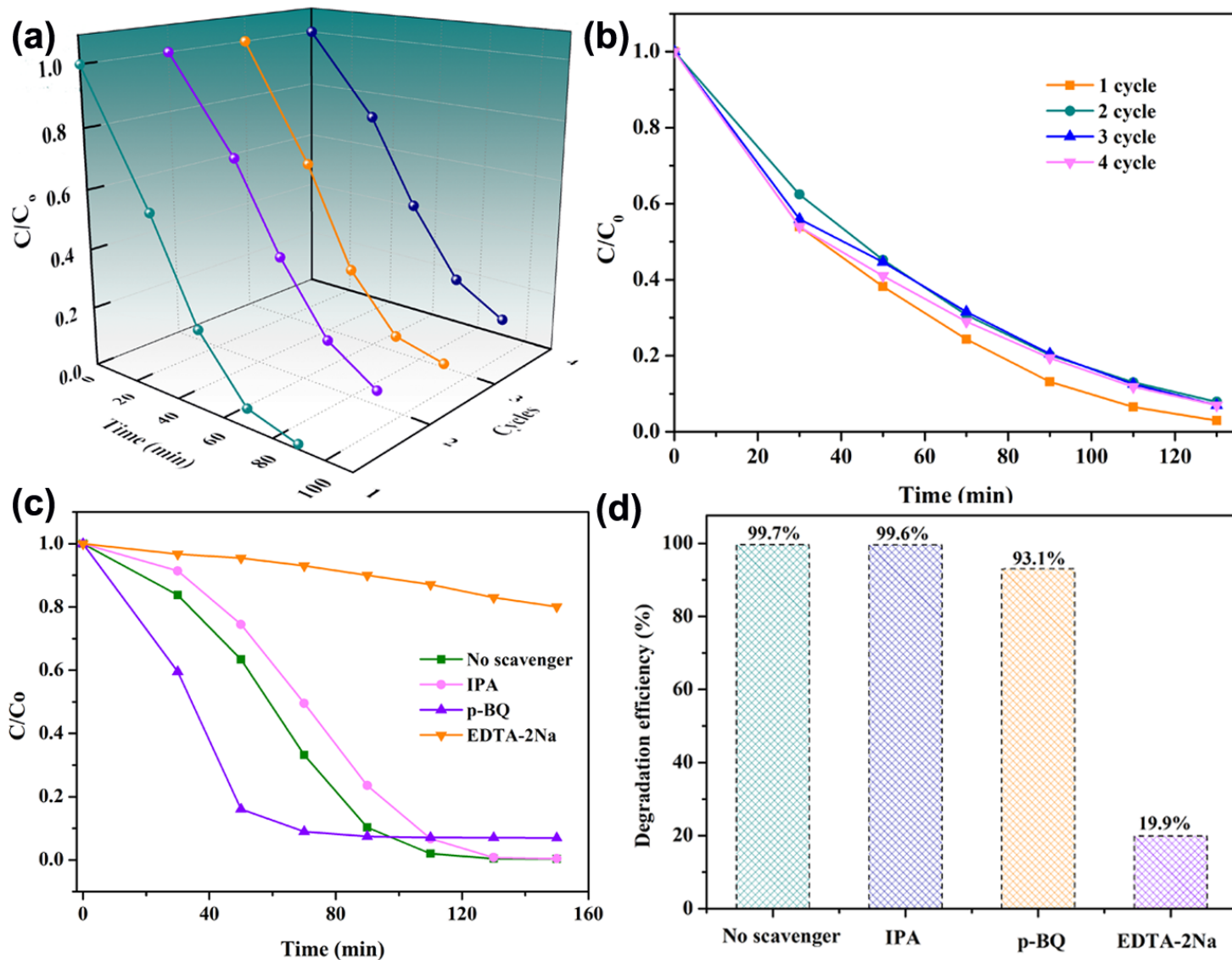


Figure 5

(a) The cyclic degradation of SH BM fabric under the visible-light irradiation; (b) the degradation curves of SH BM fabric under the outdoor natural sunlight; (c)-(d) the relevant photocatalytic degradation mechanism of Bi₂MoO₆ powder.

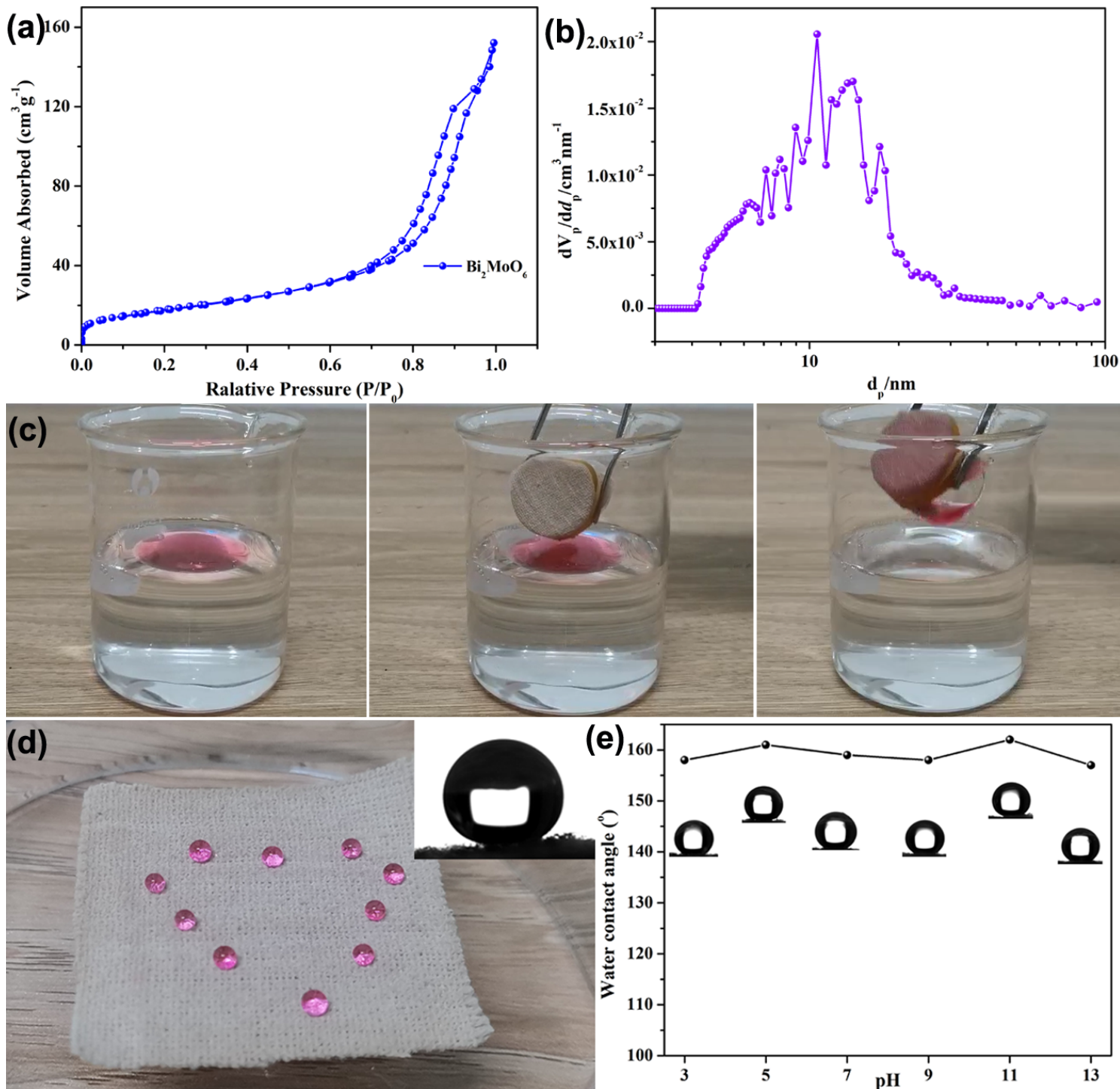


Figure 6

(a) The adsorption-desorption isotherms of Bi_2MoO_6 ; (b) the relevant distribution of pore size; (c) the removal oil phase (methylbenzene, dyed by oil red) process of SH BM fabric; (d) the water (dyed by RhB dye) behavior on the surface of SH BM fabric; (e) the water contact angle of SH BM fabric after treated in distinct acid and alkali circumstance.

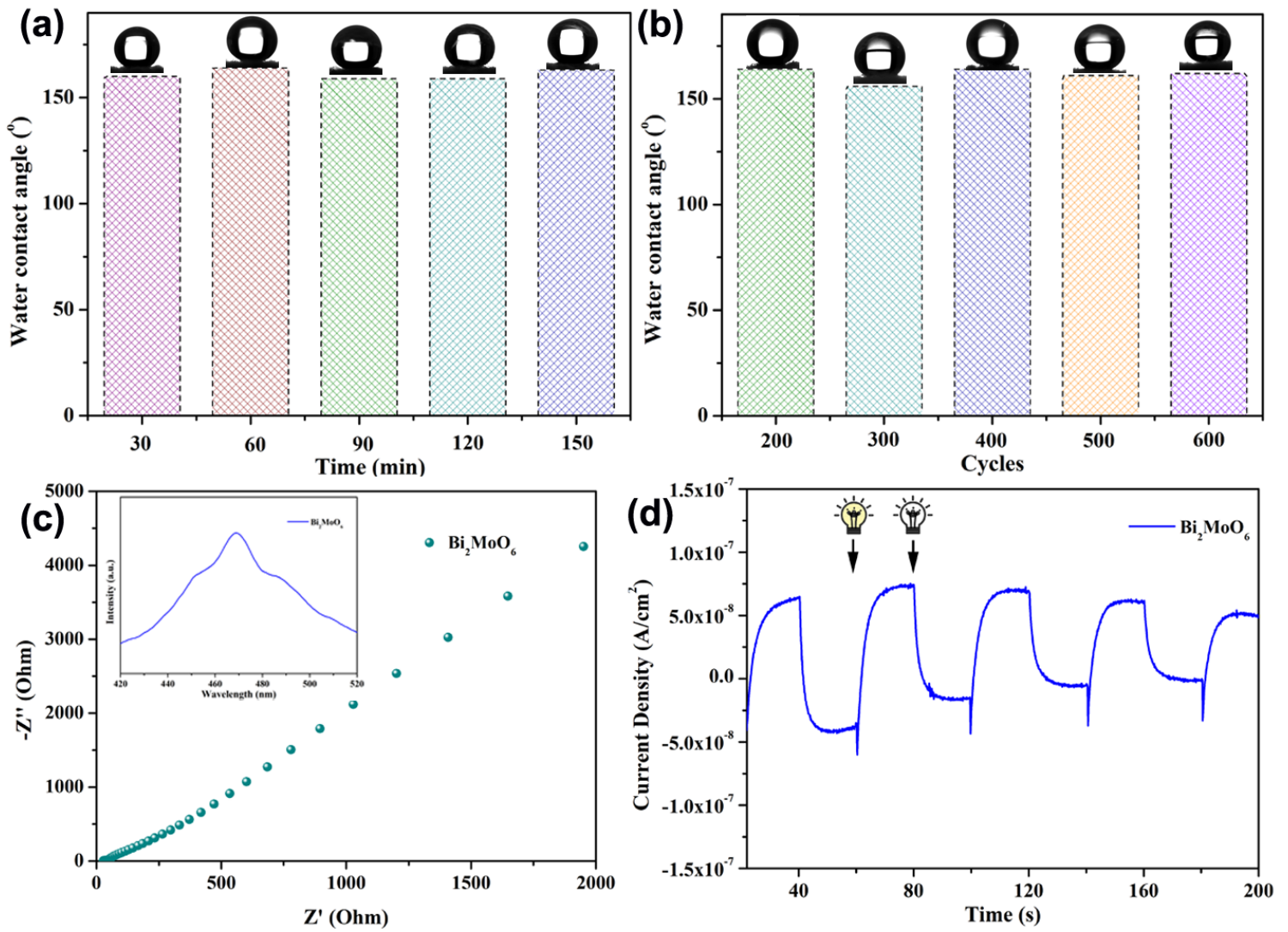


Figure 7

The superhydrophobic stability of the SH BM fabric: (a) thermal treatment at 100 °C, (b) frictional wear treatment; (c) the EIS analysis and PL spectrum of Bi_2MoO_6 ; (d) the photocurrent response of Bi_2MoO_6 powder.

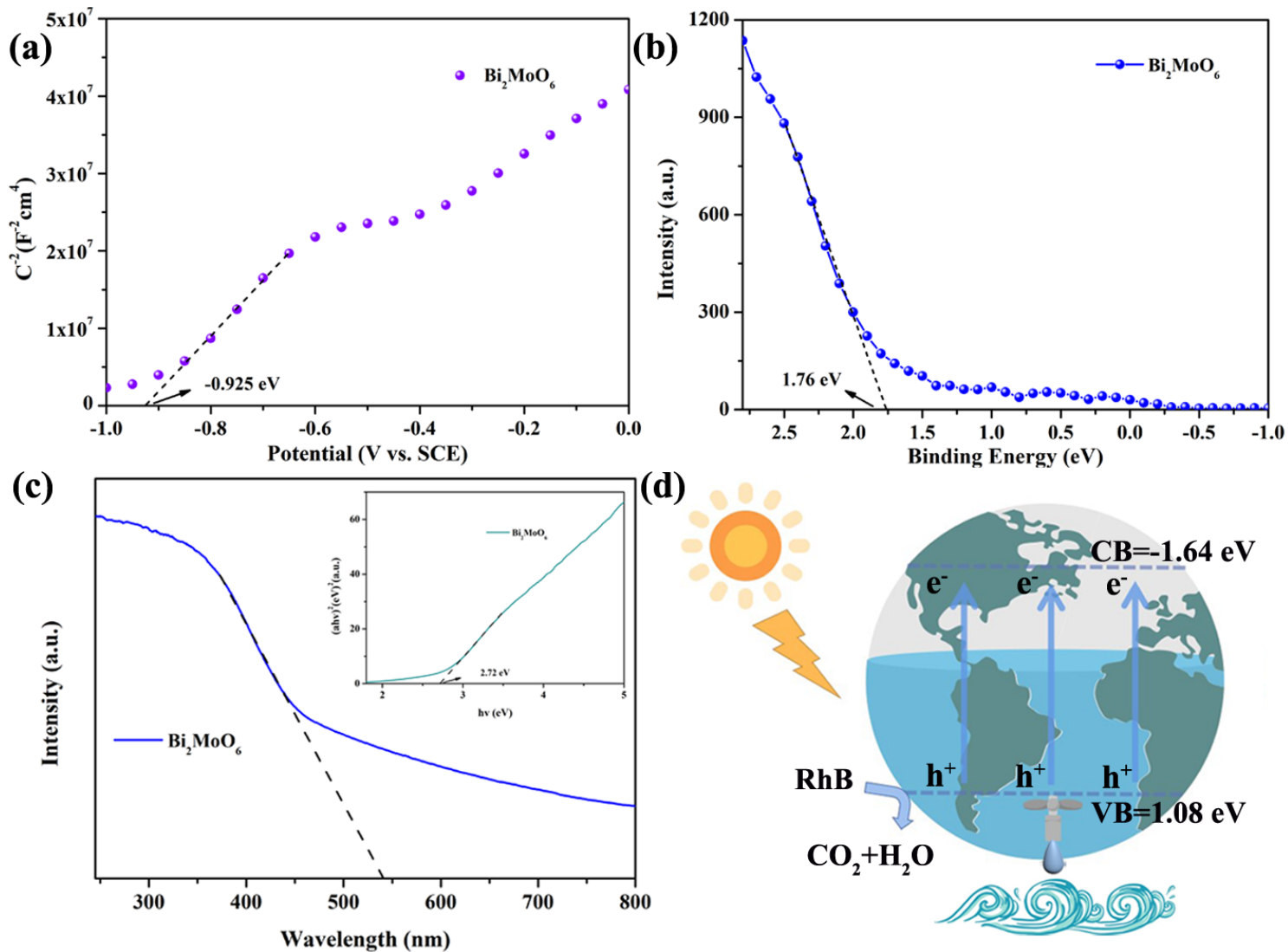


Figure 8

(a) The Mott-Schottky curves of Bi_2MoO_6 ; (b) the valence band spectra; (c) the UV-Vis diffuse reflectance spectra and $(ah\nu)^2$ versus $h\nu$ plot of Bi_2MoO_6 ; (d) the diagram of relevant degradation mechanism.